



Electrophoretic deposition of chitosan reinforced graphene oxide-hydroxyapatite on the anodized titanium to improve biological and electrochemical characteristics

N. Karimi, M. Kharaziha*, K. Raeissi

Department of Materials Engineering, Isfahan University of Technology, Isfahan, 84156-83111, Iran

ARTICLE INFO

Keywords:

Anodizing
Hydroxyapatite nanoparticles
Graphene oxide
Chitosan
Electrophoretic deposition

ABSTRACT

Chitosan reinforced hydroxyapatite-graphene oxide (CS-GO-HA) nanocomposite coatings were developed using electrophoretic deposition process in order to improve the biological and electrochemical properties of Ti surface. Moreover, the role of anodized layer on the physical and electrochemical properties of the CS-GO-HA nanocomposite coating was evaluated. After synthesis of HA-GO nanopowder using a sol-gel process, nanocomposite coatings with various concentrations of chitosan (0.5, 1 and 1.5 mg/ml) were produced. Increasing the chitosan content lowered the deposition rate of HA-GO nanoparticles, reduced the coating thickness and diminished apatite-formation ability and biocompatibility. Noticeably, MG63 cell viability significantly reduced from 119.3 ± 5.1 (% control) to 51.9 ± 14.8 (% control), when the chitosan concentration increased from 0.5 to 1.5 mg/ml. In addition, the CS-GO-HA coating containing 0.5 mg/ml chitosan revealed the best barrier property owing to the less crack formation. Furthermore, anodizing of titanium substrate and formation of TiO₂ nanotube (TiNT) resulted in the formation of crack-free and homogeneous CS-GO-HA coatings without any observable defect. Moreover, the TiNT formation noticeably improved barrier resistance of the coating (6.7 times) due to better adhesion governed between coating and substrate. Our results confirmed that the surface modification using both anodizing of Ti substrate and electrophoretic deposition of ternary CS-GO-HA nanocomposite coating with 0.5 mg/ml chitosan successfully improves electrochemical properties, bioactivity and cell function, which makes it promising for bone implant applications.

1. Introduction

Despite the wide advancement, metallic biomaterials still account as a considerable portion of clinically applied materials for various implants [1]. Among them, titanium (Ti) and its alloys are the most commonly applied materials for medical implants due to their moderately low elastic modulus, high strength-to-weight ratio and appropriate corrosion resistance, and biocompatibility [1]. Nevertheless, the inert nature of Ti alloys has led to weak bone bonding capability, and, therefore, unsatisfactory osseo-integration [1].

In the recent decades, numerous surface treatment approaches (e.g. plasma-spray [2], acid-etch treatment [3] and anodizing [4]) as well as bioactive coatings (e.g. hydroxyapatite (HA) [5], bioactive glass [6], magnesium silicates [7] and wollastonite [8]) have been developed on Ti-based samples. Among the bioactive coatings, HA (Ca₁₀(PO₄)₆(OH)₂) is the most commonly material for bone regeneration thanks to its excellent biocompatibility, osteoconductivity, and similarity with the

mineral part of bone and dentin [9,10]. However, the inferior wear resistance and fracture toughness of pure HA lead to crack propagation which reduces corrosion resistance [9,11]. In this regard, various nanocomposite coatings based on HA, consisting of polymers (such as chitosan [12], hyaluronic acid [13,14], alginate acid [15] and chitosan-heparin [16]) and carbon-based materials (such as graphene [17], graphene oxide [18], carbon nanotubes [19]) have been developed. Recently, owing to the unique structure and excellent mechanical, thermal and electrical properties as well as good bactericidal and biocompatibility, graphene-based materials have been employed for various biological applications [10,13,20]. The graphene-based materials, specifically graphene oxide (GO) nanosheets, have been applied as reinforcement agents in nanocomposites to improve mechanical characteristics [10]. Yan et al. [21] developed nanocomposite coatings consisting of GO, HA, and gelatin on TiO₂ substrate by electrochemical deposition, and concluded that the addition of GO to the composite coatings improved corrosion resistance and also biocompatibility of the

* Corresponding author.

E-mail address: Kharaziha@cc.iut.ac.ir (M. Kharaziha).

<https://doi.org/10.1016/j.msec.2018.12.136>

Received 26 May 2018; Received in revised form 7 December 2018; Accepted 29 December 2018

Available online 31 December 2018

0928-4931/ © 2018 Elsevier B.V. All rights reserved.

coating [21]. The results showed that the oxygenic functional groups presenting on the edges and planes of GO nanosheets could improve the bioactivity of the composites such as gelatin-GO [22] and PCL-GO [23]. However, the bonding strength of ceramic-graphene coatings is often weak and the porous structure of these coatings may reduce the corrosion resistance of metallic substrates [24]. Reduction of porosity in GO-ceramic coating by incorporation of a polymer phase is a promising approach to overcome this issue [12]. Chitosan, a derivative of chitin, is a polysaccharide with non-toxic characteristics, superior biocompatibility, antibacterial property, and biodegradability. Owing to the excellent properties of chitosan, various nanocomposite coatings based on chitosan have been developed [25]. Bumgardner et al. [26] developed the chitosan coating on a titanium substrate and concluded that the chitosan coatings could be used in implants for teeth, skulls, or orthopedic applications.

Various techniques consisting of sol-gel [27], plasma spraying [28] and electrodeposition [29] have been applied to develop nanocomposite coatings. Among them, electrophoretic deposition (EPD) has been considered to develop various polymer, ceramic and nanocomposite coatings owing to cost-effective, simplicity and practical design of complex constructs [30–32]. Li et al. [33] studied the EPD deposition of the GO-hyaluronic acid-HA (GO-HY-HA) nanocomposite coatings and found that the GO prevented from the formation and release of cracks in the coating and improved the corrosion resistance of Ti sample.

Despite the promising results of bioactive coatings on Ti implants, the insufficient adhesion strength between coating and Ti substrate could lead to delamination of coatings and consequently implant failure [34]. To overcome this issue, surface treatment approaches via various physical, chemical and electrochemical techniques have been applied before surface coating process [35]. Among them, anodizing process has been developed to create titania nanotube (TiNT) arrays over a Ti surface [36]. Mokhtari et al. [37] developed TiNT array on the Ti substrate using electrochemical anodizing process as an intermediate layer for chitosan-58S bioactive glass coating. The TiNT layer significantly improved surface roughness and water contact angle leading to improved bioactivity and antibacterial properties. However, according to our knowledge, the role of anodized TiNT layer on the electrophoretic deposition has not been evaluated, yet.

The aim of this research is to develop a two-layer nanocomposite coating of TiNT/GO-HA-chitosan and study its physical properties, corrosion resistance and biological characteristics. Accordingly, HA-GO nanocomposite powder was primarily synthesized by a simple sol-gel process, before the EPD process. Consequently, after preparation of TiNT on the surface of Ti via anodizing process, the EPD process was performed to coat the chitosan reinforced HA-GO on Ti substrate. In addition, we also investigated the effect of chitosan concentration (0.5, 1 and 1.5 mg/ml) and the EPD deposition processing parameters (voltage and time) on the physical characteristics as well as in-vitro bioactivity and in-vitro osteoblast-like cell responses.

2. Materials and methods

2.1. Materials

GO powder (purity > 99%, thickness: 3.4–7 nm, 6–10 layers) was prepared from Nanosay Co., Iran. Chitosan with low molecular weight, provided from Sigma-Aldrich Co., was used for coating. Calcium nitrate ($\text{Ca}(\text{NO}_3)_2 \cdot 4\text{H}_2\text{O}$), ammonium dihydrogen phosphate ($\text{NH}_4(\text{H}_2\text{PO}_4)$) and ammonium fluoride (NH_4F) were purchased from Merck Co. Commercial pure Ti (grade TA1) sheet with 1 mm thickness, supplied by Sigma-Aldrich Co., was used as the substrate. Deionized distilled (DI) water was used in all experiments.

Before the electrophoretic process, a simple chemical treatment approach was performed on the Ti sheets. In this respect, Ti samples ($20 \text{ mm} \times 10 \text{ mm} \times 1 \text{ mm}$) were polished by SiC paper (400 grits) and ultrasonically were cleaned in acetone, alcohol and deionized water

(DI), respectively, each one for 30 min and finally were activated for 3 min in $\text{HNO}_3:\text{HF}:\text{H}_2\text{O} = 30:4:70$. All other reagents and solvents of analytical grade were purchased from Sigma-Aldrich and Merck Co.

2.2. Fabrication of anodized titanium nanotubes

Anodizing process was performed according to the previous research [37]. Briefly, the titanium sheets ($20 \text{ mm} \times 10 \text{ mm} \times 1 \text{ mm}$) were grounded and polished by grit-sized SiC papers and alumina powder, respectively, and finally, were etched in acid solution ($\text{HNO}_3:\text{HF}:\text{H}_2\text{O} = 1:1:3$) for 15 s. After ultrasonication of the samples in acetone and ethanol, respectively, the anodizing process was performed in glycerol solution containing 0.5 wt% sodium fluoride (NaF) and 12.5 (v/v) % DI water. In order to perform anodizing process, Ti sheet, as the anode electrode, and platinum foil ($40 \text{ mm} \times 80 \text{ mm}$), as the cathode electrode, were 3 cm apart and connected to the positive and negative poles of a direct current (DC) power supply (HANIElectronics, HE-P35Extra, 30V-5A), respectively. Voltage and time of the anodizing process were optimized at 30 V and 1 h, respectively. After anodizing and formation of titania nanotubes (TiNT), the Ti sheets were washed with DI water and dried at room temperature.

2.3. Synthesis of hydroxyapatite (HA)-graphene oxide (GO) nanoparticles

In order to synthesize HA-GO nanopowder at a weight ratio of 45:3, 100 ml calcium nitrate solution in DI water (0.01 M) was first prepared. After formation of the homogenous solution, 0.003 g of GO was added, stirred for 20 min and consequently was sonicated for 20 min. After adjusting the pH of both solutions to 9 using dilute ammonia solution, 0.1 M ammonium dihydrogen phosphate solution was added to the calcium nitrate solution and mixed for 3 h. Finally, the resulted solution was then dried for 24 h at 70°C , and subsequently, was calcined for 1 h at 450°C .

2.4. Electrophoretic deposition of chitosan reinforced HA-GO coating

Before the EPD process, nanocomposite suspensions consisting of HA:GO nanopowder and chitosan in ethanol:water solution with a volume ratio of 80:20 were prepared. In this respect, 5 wt% suspension of HA:GO nanopowder in ethanol:water solution was primarily prepared. Separately, chitosan solution was prepared in 3% acetic acid solution. In order to evaluate the role of chitosan concentration on the coating properties, various concentrations of chitosan solution (0.5, 1 and 1.5 mg/ml) were prepared. Consequently, HA:GO suspension was mixed with chitosan solution with the volume ratio of 85:18. The pH of solution was adjusted at 4 by adding a dilute acetic acid solution.

The EPD process was conducted under continuous stirring using 30V DC power for 3 min while a stainless steel electrode (anode) and a Ti substrate (cathode), 1 cm apart were applied. The coated sample was taken out carefully from the EPD cell and dried horizontally in the air at room temperature. Finally, the coatings were cross linked using 0.5% glutaraldehyde for 3 s and then dried horizontally in the air at room temperature for 24 h. According to the chitosan concentration (0.5, 1 and 1.5 mg/ml), the samples were named as 0.5CS-30V-3 min, 1CS-30V-3 min and 1.5CS-30V-3 min, respectively.

2.5. Characterization of nanopowders and coatings

HA-GO, GO and HA nanopowders were characterized by transmission electron microscope (TEM, Philips 208S) and scanning electron microscope (SEM, Philips, XL30 SERIES). Before SEM imaging, the samples were sputter coated with a thin layer of gold. Furthermore, the average particle size was characterized using ImageJ software. Moreover, surface morphology and chemical composition of the coatings were characterized using SEM and energy dispersive X-Ray spectroscopy (EDX). The chemical composition of HA-GO, GO and HA

nanopowders and the coatings was performed using X-ray diffraction (XRD, X'Pert Pro X-ray diffractometer, Phillips, Netherlands) technique carried out with CuK α radiation ($\lambda = 0.154$ nm) at a generator voltage of 40 kV. Moreover, the crystallite size of powders was estimated using Sherrer equation (Eq. (1)):

$$L = \frac{0.89\lambda}{\beta \cos\theta} \quad (1)$$

where L is crystallite size (nm), λ is wavelength (nm) of X-ray, β is width at half maximum of peaks and θ is the angle of a specific peak (degree). Fourier transform infrared spectroscopy (FTIR, Bomem, MB 100), was applied in the range of 400–800 cm^{-1} and scanning speed of 2 cm^{-1} . The hydrophilicity of the coatings was estimated using a sessile drop method by calculating the static water contact angles on a drop-shape system. For this purpose, a droplet of 1 μl was placed on the samples and the images of droplet were taken ($n = 3$). The water contact angle was measured using the ImageJ software. At least three different points of the surface were imaged and the averages of these values were reported. The surface roughness of the samples ($n = 3$) was also estimated according to ISO 1997 standard using a mechanical contact type stylus-based surface roughness tester, Mitutoyo SurfTest SJ-210. Subsequently, R_a was measured and the average value was considered for further analysis. The adhesion strength between the coatings and the substrate was also carried out by the ASTM standard D3359 with the PAT-2000 glue on the coatings. This method was applied by pasting and then removing the glue from the surface of coating at the intersection of a grit made by five deep cuts through the coating into the substrate. Based on the number of squares taken from the surface, the adhesion was determined in a 0-5B scale. While 5B was for the best adherent coating, the edges of any square were not damaged and no square was detached from the surface, the 0B showed the worst bonding strength with all squares detached from the surface.

2.6. Electrochemical evaluation of nanocomposite coatings

Corrosion resistance of the samples was evaluated using potentiodynamic polarization and electrochemical impedance spectroscopy (EIS) technique. Electrochemical measurements of the nanocomposite coatings were conducted using a three-electrode electrochemical cell kit consisting of the coated samples as the working electrode, Ag/AgCl saturated in KCl as the reference electrode and a platinum sheet as the counter electrode. These tests were carried out using an AMETEK potentiostat model PARSTAT2273 in simulated body fluid (SBF) solution at pH 7.4. Prior to the potentiodynamic polarization, the samples were immersed in SBF for 24 h. The polarization scan was from -250 mV vs. open circuit potential (OCP) at the scan rate of 1 mV/s. For EIS measurement, the frequency range was from 10^5 Hz to 10^{-1} Hz. The results of the corrosion tests were estimated by extrapolating the polarization curve based on ASTM-G102–89.

2.7. In vitro bioactivity evaluation

In vitro bioactivity of nanocomposite coatings was examined via soaking the samples in SBF solution (pH 7.40) at 37 °C for 14 days. During soaking the samples, the pH value changes of SBF solution were measured at pre-determined time intervals using an electrolyte-type pH meter. Moreover, the apatite formation on the surface of the samples was investigated using SEM imaging and EDS analysis, as described elsewhere. Moreover, in order to compare the bioactivity of various samples, the concentration of Ca and P ions in the SBF solution was estimated using inductively coupled plasma (ICP, Perkin Elmer).

2.8. Cell culture

Biocompatibility of the coatings ($n = 3$) was evaluated using MG63 cell line from Royan Institute of Iran. The MG63 cells were cultured in

complete culture medium (DMEM-low, containing 10% (v/v) fetal bovine serum (FBS, Bioidea, Iran) and 1 (v/v) % streptomycin/penicillin (Bioidea, Iran)) at 37 °C in an atmosphere containing 5% CO_2 . The culture medium was refreshed every 3 days. Before cell culture, the samples were sterilized for 60 min in 70% ethanol and 6 h under UV light. Consequently, the samples were immersed in the complete culture medium for a day just before cell seeding. Consequently, 10^4 cells were seeded on the samples as well as tissue culture plate (TCP, control) and cell-seeded samples were incubated at 37 °C under 5% CO_2 condition for 7 days and medium was changed every 3 days.

2.8.1. Cell viability study

The relative viability of cells was studied by 3-(4,5-dimethylthiazol-2-yl)-2,5-diphenyltetrazolium bromide (MTT), according to manufacturer protocol (Sigma-Aldrich). At the specific time points, after removing the culture medium, 500 μl of MTT solution (0.5 mg/ml in a phosphate buffer solution (PBS)) was poured into each well. After 4 h incubation at 37 °C under 5% CO_2 , the formazan purple crystals were dissolve dimethyl sulfoxide (DMSO solution, Sigma). The purple solution was then placed in 96-well plates and their optical density (OD) was measured at the wavelength of 490 nm using a microplate reader (Biotech) against DMSO (blank). Finally, the relative cell viability was expressed as following [38]:

$$\text{Cell viability (\%control)} = \frac{A_{\text{Sample}} - A_{\text{Blank}}}{A_{\text{Control}} - A_{\text{Blank}}} \times 100 \quad (2)$$

where A_{Sample} , A_{blank} and A_{control} were the absorbance of the sample, blank (DMSO) and control (TCP), respectively.

2.8.2. Cell morphology study

Morphology of the cells seeded on the samples was studied using SEM technique. After 7 days of culture, the cells were fixed with 2.5% glutaraldehyde solution (Sigma) for 3 h. Subsequently, the cell-seeded samples were rinsed two times with PBS, and dehydrated in the graded concentrations of ethanol (30, 70, 90, 96 and 100 (v/v) %) for 10 min, respectively. After complete drying at room temperature, the samples were imaged using SEM.

2.8.3. Immunostaining for cell cytoskeletal organization

Immunostaining was performed to assess the effect of the surface coating on the cytoskeletal organization (F-actin) of MG64 cells after 7 days of culture. After 30 min-fixation of the cell-seeded samples in 4% (v/v) paraformaldehyde (Sigma) at room temperature, they were permeabilization in 0.1% Triton X-100 (Sigma) for 5 min. Consequently, the cell-seeded samples were blocked in a 2% bovine serum albumin (Sigma) solution in PBS for 1 h. After two times rinsing with PBS, the samples were incubated in a 1:40 dilution of rhodamine phalloidin (Cytoskeleton, USA) solution for 30 min to stain the actin filaments. Subsequently, cell nuclei were stained with a 1:1000 dilution of 4',6-diamidino-2-phenylindole dihydrochloride (DAPI, Sigma) in PBS for 5 min. Finally, the samples were visualized using a confocal microscope (Leica TCS SPE, Wetzlar, Germany).

2.9. Statistical analysis

The cell culture data in this study were examined using one-way ANOVA analyses and the least significant difference test and reported as mean \pm standard deviation (SD). To determine a statistical significance between groups, Tukey-Kramer post-hoc test using GraphPad Prism Software (V.6) was applied and P -value < 0.05 was defined as statistically significant.

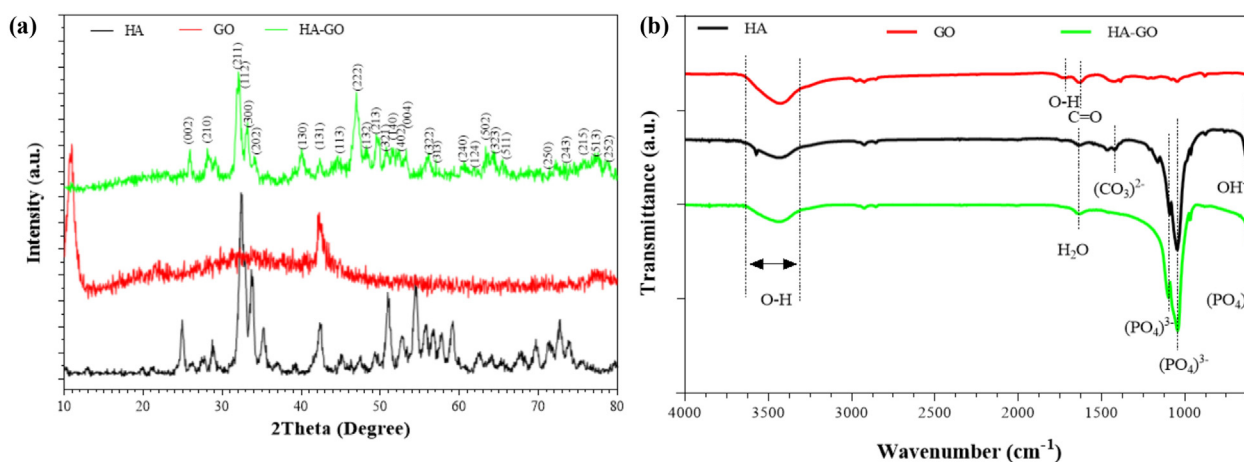


Fig. 1. (a) XRD patterns as well as (b) FTIR spectra of GO, HA and HA-GO nanopowders.

3. Results and discussion

3.1. Characterization of HA-GO nanopowder

Using the EPD process, the co-deposition of multi-components was a complex approach, thus, HA-GO nanopowder with the weight ratio of 45:3 was in-situ synthesized, at first. The weight ratio between these two components was optimized via preliminary experiments. XRD patterns of the HA-GO nanopowder as well as GO and HA, synthesized in a similar approach, are presented in Fig. 1a. The XRD pattern of pure HA powder revealed a good correlation with the standard HA phase with reference code 01-074-1243 showing that the HA was pure and single-phase. Moreover, crystallite size of the HA nanopowder estimated according to the Scherrer equation was about 26 nm. Furthermore, the XRD pattern of GO nanosheets consisted of a peak centered at $2\theta = 11.1^\circ$ corresponding to the (001) plane and $2\theta = 42.5^\circ$ relating to the (100) plane [33,39]. Moreover, the XRD pattern of HA-GO nanopowder consisted of the main characteristic peak of HA at $2\theta = 31.8^\circ$, without any secondary phase. Furthermore, the characteristic peaks relating to GO component could not be detectable in the XRD pattern of HA-GO nanopowder, which might be due to the low concentration of GO owing to the ultrasonic dispersion of solution during the synthesizing process. Similarly, Li et al. [33] showed that the GO characteristic peak was not detected at GO-hyaluronic acid-HA nanocomposite coatings due to its less crystallographic order. The crystallite size of HA in the HA-GO nanopowder was similarly calculated around 28 nm showing that the GO nanosheets did not play a significant role in the nucleation and growth of HA nanopowder.

In order to confirm the presence of HA and GO in the synthesized HA-GO nanopowder, FTIR spectroscopy was applied (Fig. 1b). The FTIR spectrum of GO consisted of the peaks centered at 1630 cm^{-1} and 1730 cm^{-1} relating to the C–O band (carboxylic group) and the OH bond, respectively. Moreover, the peaks range of $3300\text{--}3700\text{ cm}^{-1}$ was related to OH⁻ group in GO nanosheets. In another word, the FTIR spectrum of HA consisted of the absorption bands at 610, 1037 and 1091 cm^{-1} related to PO_4^{3-} functional group. In addition, the peaks centered at 636 cm^{-1} , 1430 cm^{-1} and 1640 cm^{-1} corresponded to the hydroxyl group (OH⁻), the carbonate group (CO_3^{2-}) and the absorption of water by the HA powder, respectively [11,40]. At this spectrum, the peaks related to the carbonate group (CO_3^{2-} at 1430 cm^{-1}), and hydroxyl group (at 636 cm^{-1} and 1730 cm^{-1}) were not detected in the in-situ synthesized HA-GO nanopowder. However, the peak that found in the 1730 cm^{-1} , related to the GO, was observed in the synthesized powder, confirming the presence of GO in HA-GO nanopowder.

In order to assess the role of GO nanosheets on the morphology of

HA-GO nanopowder, SEM and TEM images of the samples were obtained. The SEM image of GO nanosheets (Fig. 2a) consisted of smooth surfaces with folded shapes at the edges. The TEM image of GO nanosheets (Fig. 2b) also showed two-dimensional sheets with ripples and wrinkles which seems to be placed side by side with a small force. Furthermore, HA nanopowder (Fig. 2c) consisted of spherical particles agglomerated to form clusters with a size of about 0.5–1.5 μm . This morphology was similarly reported in previous researches [41]. The agglomeration of HA particles could be due to their high surface energy [42]. Moreover, the TEM image of HA nanopowder (Fig. 2d) confirmed the formation of HA nanopowder with spherical morphology and average particle size of $29 \pm 3\text{ nm}$. After combination of the GO nanosheets and HA nanopowder, the morphology of HA nanoparticles did not significantly change (Fig. 2e). The results showed that the HA nanopowder distributed on the sheets with few agglomerations. According to TEM image (Fig. 2f), the synthesized powder consisted of HA nanoparticle embedded in the GO nanosheets to form particles with average size of $33.6 \pm 5.3\text{ nm}$.

3.2. Characterization of nanocomposite coatings on Ti substrate

After successful synthesis of HA-GO nanoparticles, nanocomposite coatings consisting of various amounts of chitosan concentrations (0.5, 1 and 1.5 mg/ml) were deposited on the chemically treated Ti sheets. Fig. 3a shows the SEM images of nanocomposite chitosan reinforced HA-GO nanopowder consisting of various amounts of chitosan. All coatings consisted of HA-GO nanoparticles which uniformly distributed on the whole surface. Moreover, the chitosan covered surface of the nanoparticles and filled the pores. However, increasing the chitosan content resulted in a lower deposition rate of HA-GO nanoparticles which might be due to the enhanced viscosity of electrolyte leading to lower mobility of the particles. Similarly, Mahmoodi et al. [11] reported an optimized concentration of viscosity for obtaining the maximum deposition rate of particles. Moreover, increasing the chitosan concentration resulted in the formation of micro-cracks which could be clearly detected in 1.5CS-30V-3 min sample. It might be due to enhanced water absorption with increasing the chitosan content which its evaporation process could lead to the formation of cracks in the coatings [43].

Cross-section images of the nanocomposite coatings (Fig. 3b) clearly showed the formation of coatings with various thicknesses, depending on the chitosan content. Increasing the concentration of chitosan from 0.5 to 1 and 1.5 mg/ml resulted in the reduced thickness of coatings from 34.7 ± 9.1 to 29.8 ± 4.7 and $16.4 \pm 5.7\text{ }\mu\text{m}$, respectively, confirming the role of chitosan on increasing the viscosity of electrolyte solution which led to less movement of HA-GO nanoparticles, and

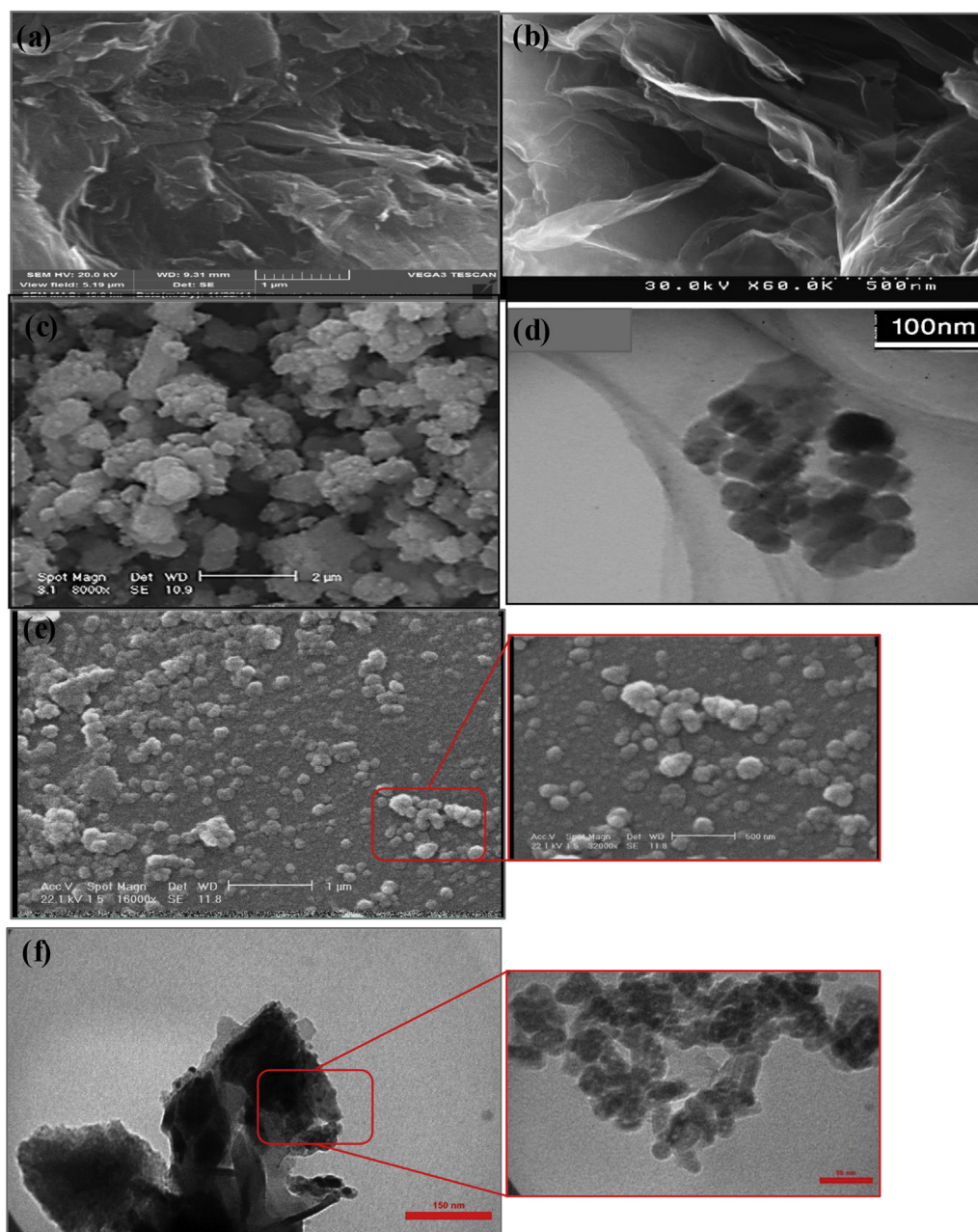


Fig. 2. SEM and TEM images of GO (a and b), HA (c and d) and HA-GO nanoparticles (e and f).

hence, more difficult precipitation on the Ti substrate. Moreover, detachment of the coating from substrate could be observed at higher chitosan concentrations (i.e. 1 and 1.5 mg/ml of chitosan), more possibly due to the inability of chitosan to provide strong interaction with the substrate. Additionally, according to Fig. 3c, the average pore size of the coatings slightly reduced with increasing chitosan concentration which could be due to filling the pores with chitosan particles. However, the difference between the average pore size of samples was not significant ($P > 0.05$). XRD patterns of the nanocomposite coatings (Fig. 3d) confirmed that whole coatings consisted of HA component. In addition to Ti characteristic peaks at $2\theta = 35.3^\circ$, and 70.8° , HA peaks could be detected as the main phase. However, due to the disordered structure of GO nanosheets and amorphous nature of chitosan, these two components could not be clearly detected in the patterns. Yang et al. [49] similarly reported that the characteristic peaks of GO could not be detected in the XRD pattern of chitosan-GO nanocomposite coating, demonstrating the formation of the fully exfoliated structure of

GO sheets in the polymer matrix and the disappearance of the regular and periodic structure of GO. EDX-mapping analysis of 0.5CS-30V-3 min sample (Fig. 4a) also clearly confirmed that calcium and phosphorus ions with atomic ratio of 1.68 were uniformly distributed in whole surface of the coating. Moreover, FTIR spectrum of 0.5CS-30V-3 min (Fig. 4b) showed that the nanocomposite coating consisted of the main characteristic peaks of all components, confirming the presence of GO, HA, and chitosan in the coating. Noticeably, the presence of a peak at 1630 cm^{-1} confirmed the presence of GO in the coating. Moreover, due to the interaction between GO and chitosan, and the deformation of O–H bond in water, no peak was observed in the nanocomposite coatings at 1730 cm^{-1} [44].

In addition to coating thickness and pore size, the chitosan concentration revealed a significant effect on the surface roughness and water contact angle (Table 1). The results revealed that the surface roughness (R_a) significantly enhanced (around 5 times) after electrophoretic deposition. Moreover, increasing the chitosan concentration

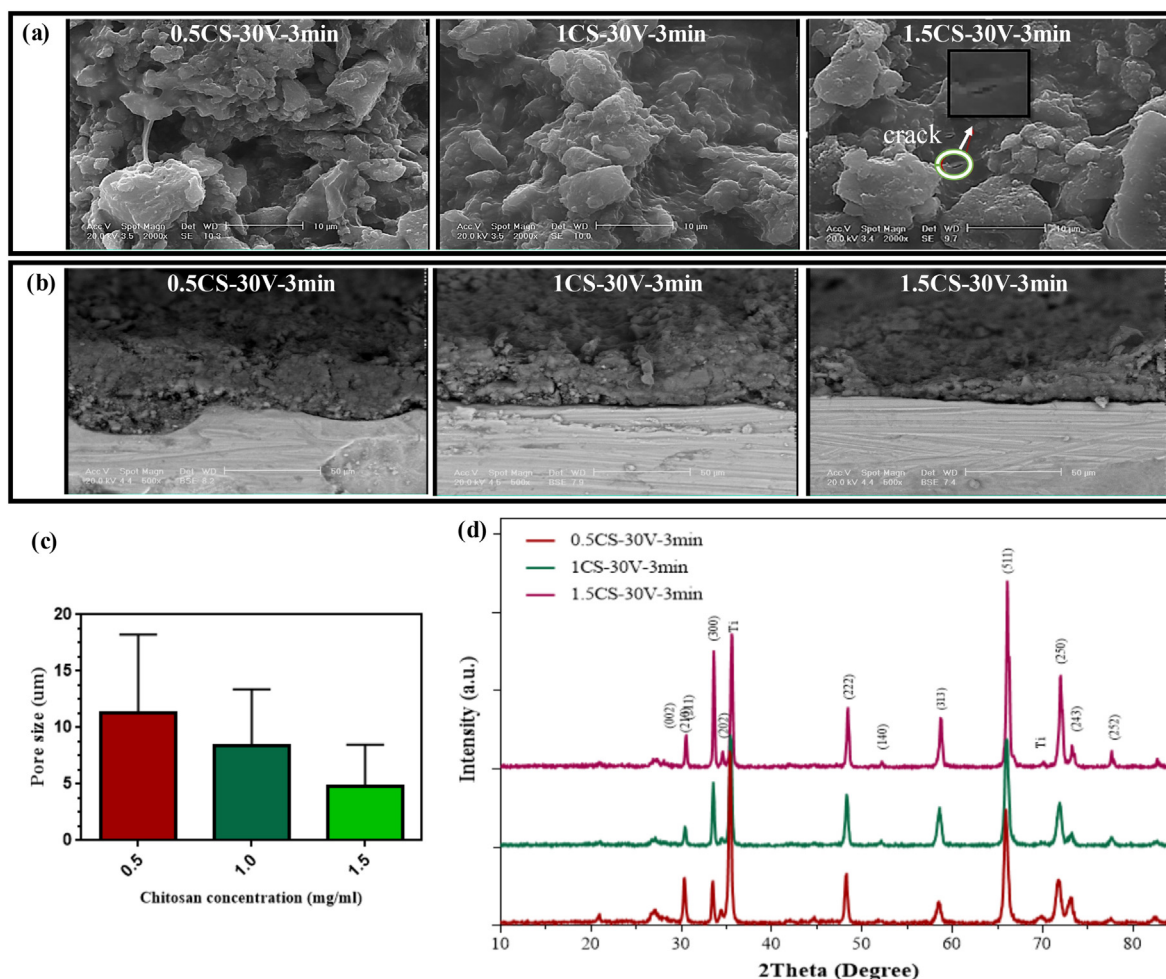


Fig. 3. SEM images of surface (a) and cross-section (b) of the coatings containing various amounts of chitosan. (c) The changes of average pore size of the coatings as a function of chitosan content. (d) XRD patterns of the coatings containing various concentrations of chitosan.

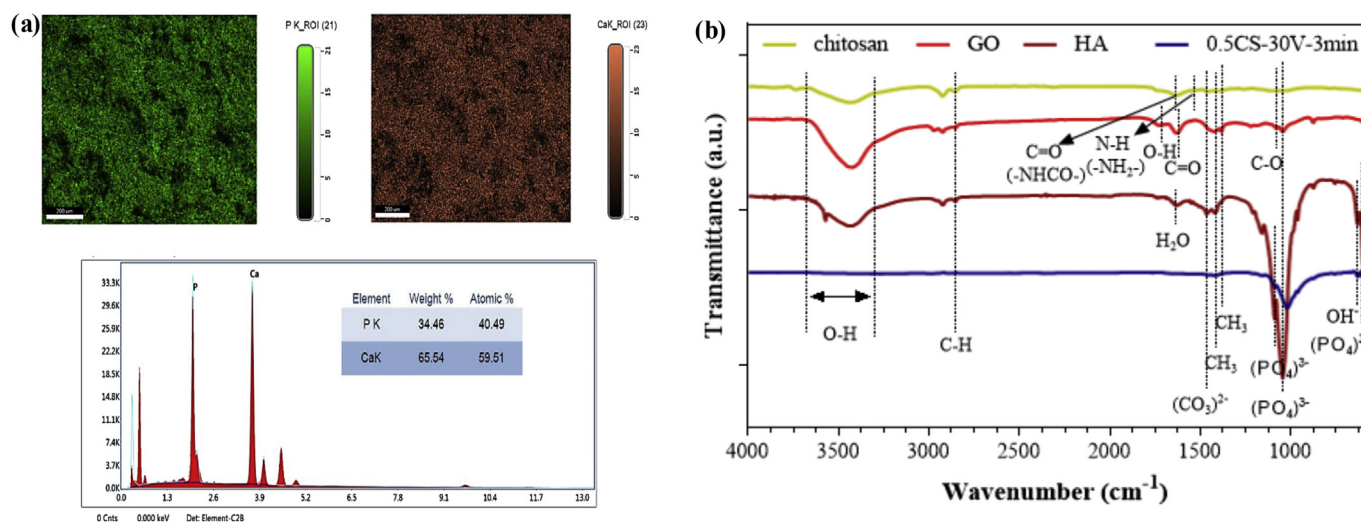


Fig. 4. (a) EDX-mapping analysis of 0.5CS-30V-3 min coating showing well distribution of HA in the coating. (b) FTIR spectra of 0.5CS-30V-3 min coating as well as GO, chitosan and HA nanopowder.

resulted in a reduction of surface roughness (1.4 times). It might be due to the role of chitosan concentration on the reduced deposition of HA-GO nanoparticles on the surface. This result was similarly reported in previous researches. For instance, Ordikhani et al. [20] studied the GO/chitosan film and observed that the surface roughness increased with

the addition of GO to the chitosan polymer matrix. Furthermore, thanks to the hydrophilic nature of chitosan, increasing the chitosan content resulted in enhanced wettability of the coatings. Our results demonstrated that the water contact angle of Ti substrate ($75.2 \pm 3.2^\circ$) significantly reduced to $69.8 \pm 3.7^\circ$ for 1.5CS-30V-3 min sample). The

Table 1
Average surface roughness (μm) and water contact angle of various samples
(*: Significant difference compared to. * $P < 0.05$).

Sample name	$R_a(\mu\text{m})$	Water contact angle ($^\circ$)
Ti	0.47 ± 0.02	75.2 ± 3.2
0.5CS-30V-3 min	$2.33 \pm 0.13^*$	73.6 ± 2.6
1CS-30V-3 min	$2.11 \pm 0.68^*$	71.8 ± 1.6
1.5CS-30V-3 min	1.58 ± 0.32	69.8 ± 3.7

improved surface roughness and hydrophilicity of the coatings could result in better protein absorption at the surface and as a result, increased cellular adhesion and cell proliferation and consequently bone formation [45].

Bioactivity is a critical factor in determining bone growth on the implant surface that prevents implant loosening [46]. The ability to form bone-like apatite on the implant surface in SBF can predict the biological function of the substances in the body [47]. SEM images of the samples after 14 days soaking in SBF solution are presented in Fig. 5a. The results showed that while the bioactivity of Ti substrate was poor, nanocomposite coatings significantly promoted the bioactivity of samples. The surface of nanocomposite coated samples was covered with spherical deposits relating to the bone-like apatite. However, the surface density of this layer enhanced with reduction of chitosan content in the coating. The pH changes of SBF solution during soaking the samples are presented in Fig. 5b. The pH value of SBF solution, exposed to the nanocomposite coated samples, revealed a decreasing trend which then went up and reached the initial pH value. This change in the overall pH value of SBF solution could be due to the presence of chitosan in the coatings. In the early stages, the dissolution of chitosan reduced pH owing to its acidic products of degradation, as similarly reported for other coatings consisting natural polymers (such as gelatin [48]). At the second week of soaking, an increase in pH value of the SBF solution was detected, which might be due to the dissolution of HA. At this time, the alkaline ions in the sample, such as calcium ions from HA, exchanged with hydronium ion (H^+ and H_3O^+) resulted in the formation of Ca-OH layer on the surface. Reduction of H^+ ions in the solution resulted in enrichment of SBF solution with OH^- ions which increased the pH value. After this step, the penetration of calcium ions (Ca^{2+}) and phosphate (PO_4^{3-}) to the surface samples resulted in higher crystallization and growth of the CaO- P_2O_5 -rich amorphous layer which consequently led to the formation of bone-like apatite sediments

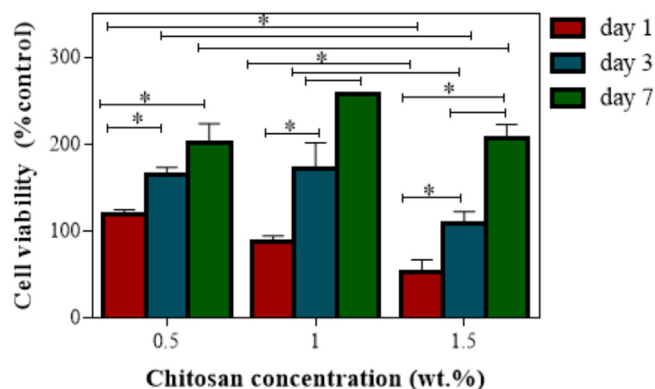


Fig. 6. Viability of MG63 cells estimated on the samples containing 0.5, 1 and 1.5 mg/ml chitosan (0.5CS-30V-3 min, 1CS-30V-3 min and 1.5CS-30V-3 min) for 1, 3 and 7 days of cultivation (* $P < 0.05$). (For the interpretation of the references to colour of this figure legend, the reader is referred to the web version of this article.)

[49,50]. To evaluate the calcium and phosphorus ions in SBF solution after immersing the samples for 14 days, ICP test was performed (Fig. 5c). Compared to the concentration of calcium and phosphorus ions in the SBF solution (100 and 31 mg/l, respectively), the calcium ion concentration of SBF solution increased slightly. However, increasing the chitosan content of the coatings results an increase of Ca ion concentration in the SBF solution. Moreover, the concentration of phosphorus ions in the coating decreased with increasing the chitosan coating. Furthermore, the concentration of calcium and phosphorus in the SBF solution in contact with Ti decreased slightly. The general trend governing bioactivity evaluation in the SBF solution is the competition between dissolution and re-sedimentation processes. Therefore, according to our results, the nanocomposite coated sample containing 1.5 mg/ml chitosan showed higher calcium solubility than others, owing to the presence of micro-cracks. These micro-cracks led to an increased surface reactivity and release of more ions from the coating to the surrounding environment.

In order to evaluate the role of chitosan concentration on the cell behavior, MTT assay was performed (Fig. 6). The results showed that the proliferation of MG63 cells seeded on all samples significantly enhanced from day 1 to day 7 ($P < 0.05$). Noticeably, the viability of MG63 cells on the 1CS-30V-3 min sample significantly enhanced from

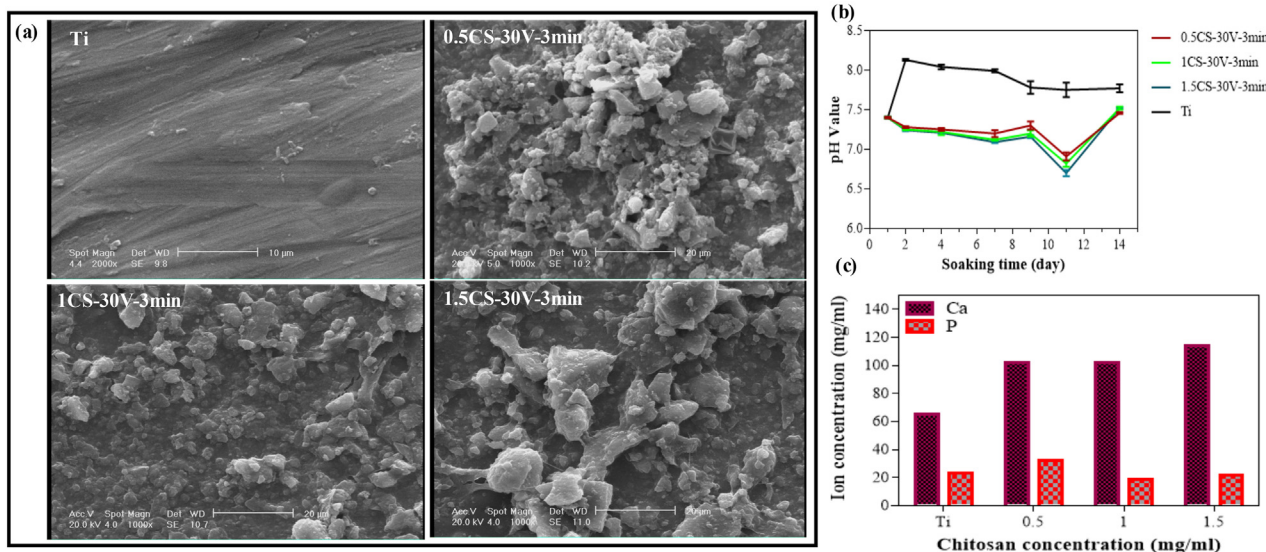


Fig. 5. (a) SEM images of Ti substrate and coated samples after immersion in SBF solution for a period 14 days. (b) pH changes of the SBF solution during the soaking of samples. (c) The concentration of Ca and P ions in the SBF solution after 14-day soaking of samples containing various concentrations of chitosan.

88.3 ± 5.7 (% control) (at day 1) to 257.2 ± 1.2 (% control) (at day 7). However, our result showed that the cell viability significantly reduced from 119.3 ± 5.1 (% control) to 51.9 ± 14.8 (% control), after the first day of culture, when the chitosan concentration increased from 0.5 to 1.5 mg/ml ($P < 0.05$). It could be concluded that cell attachment reduced with increasing chitosan concentration. Moreover, compared to the control sample (TCP), the viability of cells on the samples was significantly improved. For instance, after 7 days of culture, the viability of cells on 1CS-30V-3 min sample was noticeably (2.6 times) greater than the control sample. It might be due to the stimulatory role of GO, HA and chitosan on the cell proliferation. Shi et al. [40] showed the effective role of HA on improvement of MG63 proliferation. In another study, Ordhikhani et al. [20] revealed that the presence of GO up to 30 wt% resulted in improved proliferation of cells. Furthermore, our results revealed that after 7 days of culture, the viability of cells on at 1CS-30V-3 min sample was significantly enhanced compared to other samples ($P < 0.05$). It might be due to simultaneous role of chemical and physical properties of this sample on the cell attachment and proliferation.

The morphology of cells cultured on the samples for 7 days, was also investigated using SEM imaging (Fig. 7a). MG63 cells were attached and spread on the surface of all specimens. According to high magnification images, with increasing the chitosan concentration up to 1 mg/ml, cell spreading is significantly improved. However, more increasing of the chitosan concentration (1.5 mg/ml) resulted in less cell spreading. In this sample, the MG63 cells with spherical morphology (indicated by red circle) could be detected on the surface, indicating the lower cell adhesion to the coating. We also investigated the actin cytoskeletal organization of MG63 cells on the various nanocomposite coated samples after 7 days of culture (Fig. 7b). Our results confirmed that the cell cytoskeletal organization was noticeably depended on the coating properties. While increasing the chitosan concentration upon 1 mg/ml noticeably improved cell attachment and spreading, the cell

surface area reduced at 1.5CS-30V-3 min sample. Cells grown on the 1CS-30V-3 min sample revealed more extended cytoskeleton which could be contributed to promoted cell attachment and consequently proliferation. Between various samples, less cells were attached and spread on the surface of 1.5CS-30V-3 min samples confirming MTT results.

EIS analysis was performed on the uncoated Ti and nanocomposite coated samples and, consequently, the Nyquist and Bode plots were drawn (Fig. 8a and b). All curves revealed one time constant. However, for better fitting, an equivalent circuit with two-time constants was applied [10,51]. Therefore, the proposed equivalent electrical circuit has two parallel time constants (Fig. 8c), where each time constant consisted of a resistance (R) and a constant phase element (CPE). The CPE, which actually replaces the ideal capacitor (C), was due to the presence of porosity, heterogeneity and possible cracks in the coating [52]. The time constant described by (CPE_b-R_b) was related to the diffusion barrier action of the oxide passive film, which is primarily formed on Ti substrate. By applying the composite coatings, the electrical elements of CPE_b and R_b (Table 2) were increased due to the further diffusion barrier action provided by the coating layers. However, the coating layers have not shown additional time constant because of their porous structure which cannot strongly prevent the penetration of aggressive ions. On the other hand, the time constant presented as (CPE_i-R_i) was used for raising the accuracy of fitting. It is believed that the CPE_i is related to the interface between the oxide passive layer and Ti substrate, while the R_i is determined by the resistance of charge transfer [51]. The values obtained by the selected circuit are presented in Table 2. According to the obtained results, due to the higher resistance of the barrier layer (R_b) compared to the interface (R_i), the corrosion performance of the coatings was mainly determined by the barrier layer resistance. Moreover, the sum of R_b and R_i indicating the total resistance of the coating (R_{tot}), demonstrated that the 0.5CS-30V-3 min coating showed the highest Faradic resistance.

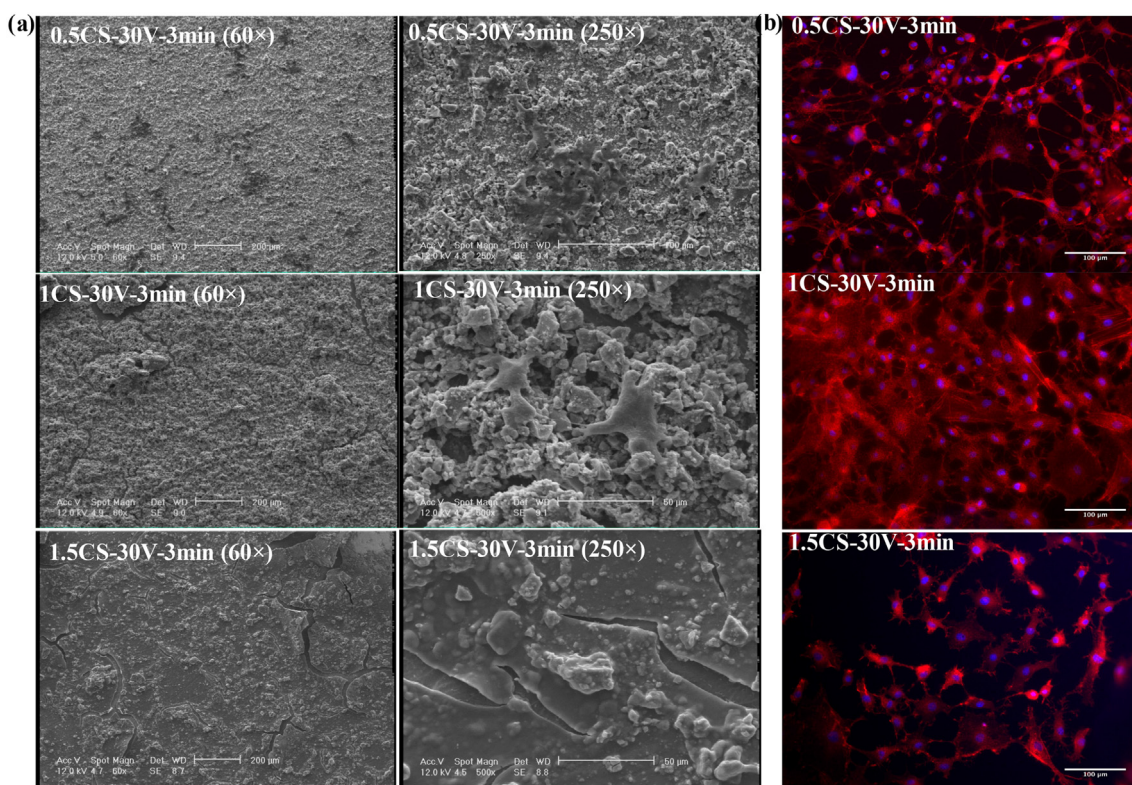


Fig. 7. a) SEM images (at two different magnifications) and b) Fluorescence microscopy images of the phalloidin/DAPI stained MG63 cells cultured on the Ti coated samples containing 0.5 (0.5CS-30V-3 min), 1 (1CS-30V-3 min) and 1.5 mg/ml (1.5CS-30V-3 min) chitosan, after 7 days of culture. (For interpretation of the references to colour in this figure legend, the reader is referred to the web version of this article.)

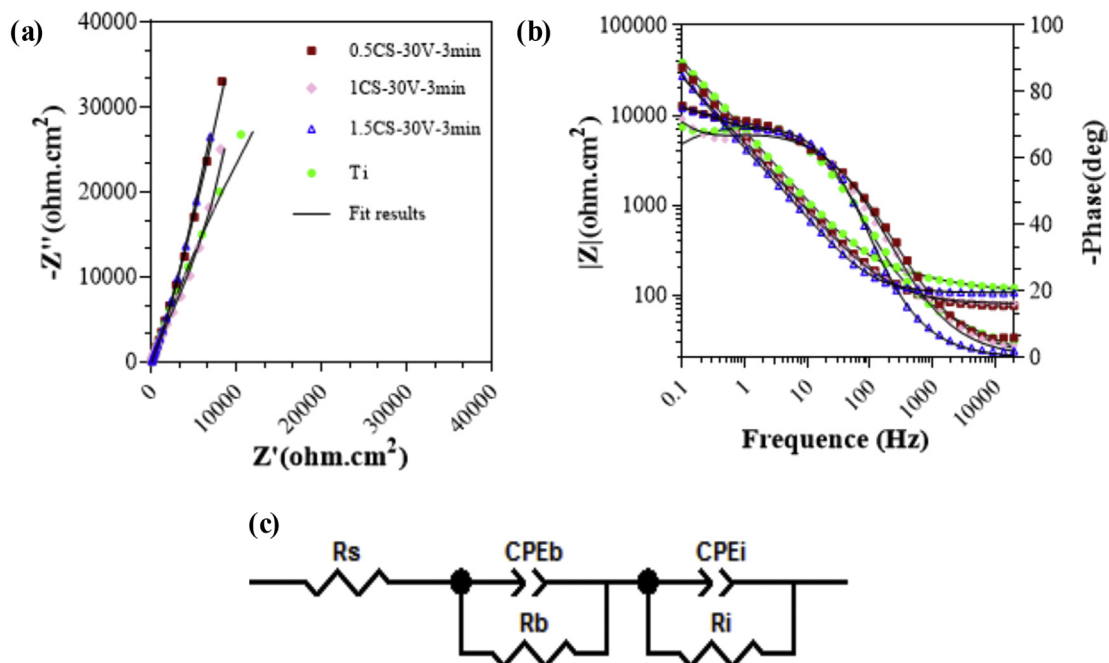


Fig. 8. (a) Nyquist, (b) Bode plots of Ti and nanocomposite coated Ti samples and c) equivalent electrical circuit obtained from Zview software for various coated samples.

Table 2

Parameters obtained from EIS test of the coatings on Ti substrate by fitting using the equivalent circuit.

Sample name	Barrier layer			Interface of metal/passive film			R _{tot} (MΩ.cm ²)	χ ² (× 10 ⁻³)
	n _b	CPE _b -T (μF cm ⁻² s ^{n_b-1})	R _b (MΩ.cm ²)	n _i	CPE _i -T (μF cm ⁻² s ^{n_i-1})	R _i (kΩ.cm ²)		
0.5CS-30V-3 min	0.94	53.42	33.01	0.64	129.69	18.02	33.01	0.66
1CS-30V-3 min	0.99	77.33	19.79	0.71	80.06	42.93	19.79	1.94
1.5CS-30V-3 min	0.88	55.64	2.97	0.75	184.12	1.72	2.97	0.34
Ti	0.79	34.55	0.32	0.73	30.30	0.05	0.32	1.77

According to the Bode-angle diagrams (Fig. 8b), the plateau region at low frequencies (around 70°) for the coating containing 0.5 mg/ml chitosan (0.5CS-30V-3 min) is higher than others, indicating better diffusion barrier effect. By the formation of cracks at higher chitosan content, the SBF solution could easily penetrate in the coating leading to create localized corrosion. Furthermore, the electrochemical evaluation of the coated samples revealed that the barrier layer resistance of all coatings was higher than that of Ti substrate confirming that all the nanocomposite coatings have improved the barrier property of samples in the SBF solution due to the reinforcement of primarily formed passive layer of Ti substrate. This behavior has been similarly reported in ref. [10].

Corrosion behavior of the coatings was also investigated using potentiodynamic polarization test (Fig. 9). The passivation current density (i_p) and corrosion potential (E_{corr}) are presented in Table 3. The results showed that all the specimens exhibited better corrosion behavior (lower current density and higher potential) than Ti substrate. However, among the coatings, the nanocomposite coating containing 0.5 mg/ml chitosan (0.5CS-30V-3 min) revealed a passive current density of about 21 nA/cm² which was significantly lower than that of the Ti with a current density of about 200 nA/cm². The lower penetration of the corrosive solution into the coating resulted in improved passivation behavior as indicated by an increase in the slope of the anodic branch. However, after the passivation behavior, a breakdown potential (E_b) could be observed where the localized corrosion of the substrate initiated. It is clear from the curves that, the 0.5CS-30V-3 min sample

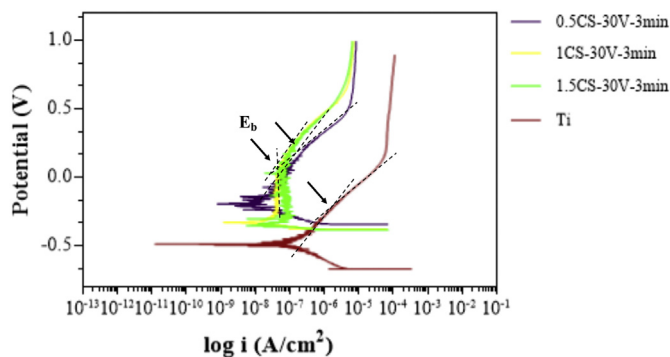


Fig. 9. Potentiodynamic polarization plots of Ti and nanocomposite coated Ti samples.

Table 3

Passivation current density, corrosion potential and breakdown potential of the coating on Ti substrate.

Sample name	i _p (nA.cm ⁻²)	E _{corr} (V vs. SCE)	E _b (V vs. SCE)
0.5CS-30V-3 min	21	-0.2	0.13
1CS-30V-3 min	47	-0.33	0.11
1.5CS-30V-3 min	80	-0.35	0.10
Ti	200	-0.48	-0.22

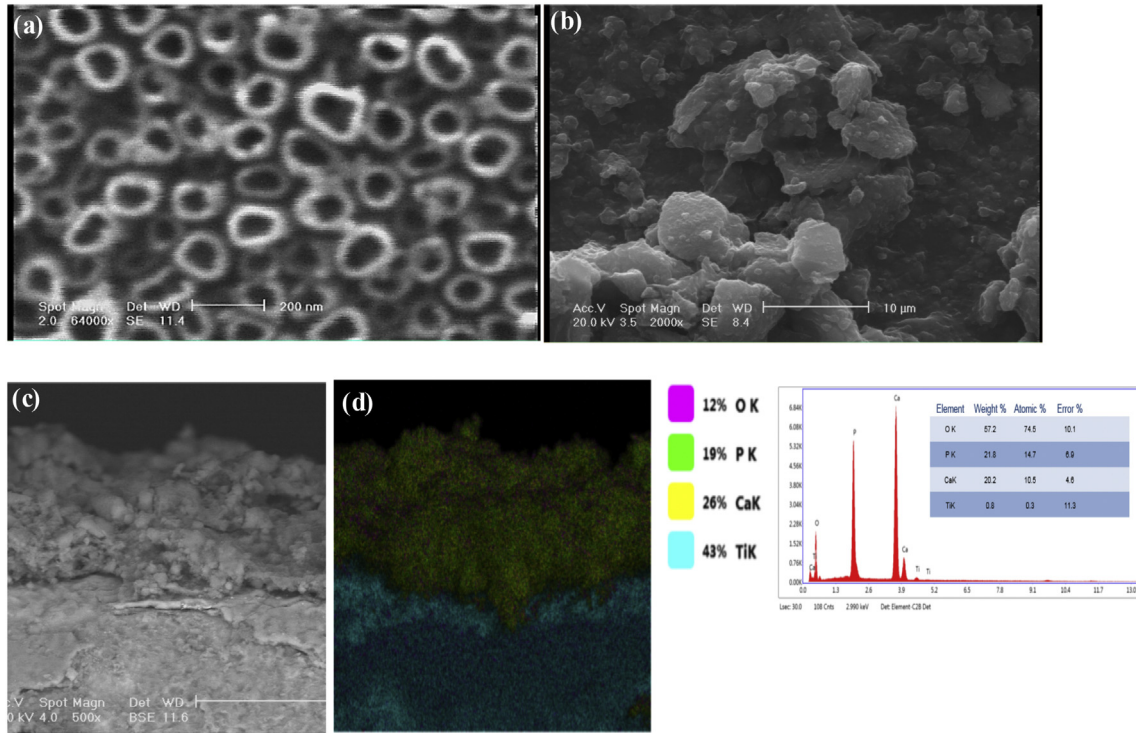


Fig. 10. (a) SEM image of anodized Ti consisting of titanium nanotube (TiNT), (b) SEM images of surface, (c) cross-section of the anodized 0.5CS-30V-3 min and (d) EDX-mapping of anodized 0.5CS-30V-3 min coated sample showing well distribution of HA nanoparticles.

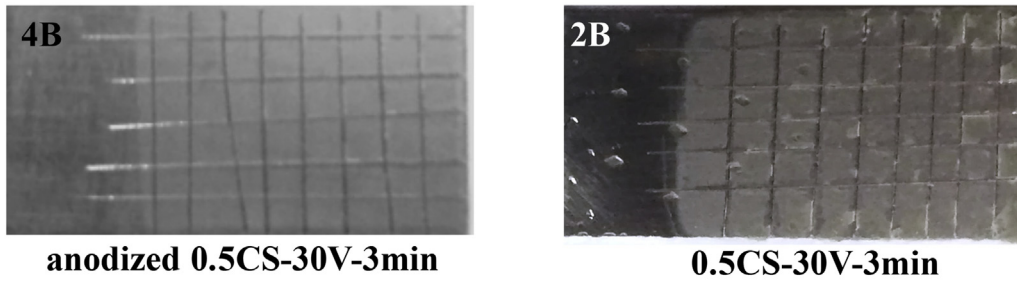


Fig. 11. The representative surface macrostructure of 0.5CS-30V-3 min and anodized 0.5CS-30V-3 min coupons after adhesion test.

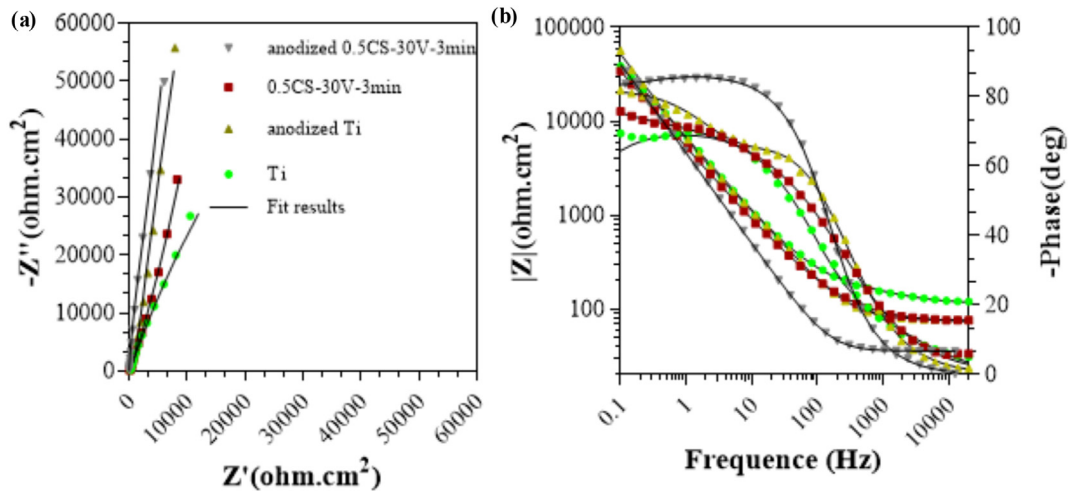


Fig. 12. (a) Nyquist and (b) Bode plots of the anodized 0.5CS-30V-3 min coated sample compared to the anodized Ti, 0.5CS-30V-3 min and pure Ti.

Table 4
Parameters obtained from EIS test of the anodized Ti and the coatings on anodized Ti substrate by fitting using the equivalent circuit.

Sample name	Barrier layer			Interface of metal/passive film			R_{tot} ($M\Omega\text{cm}^2$)	χ^2 ($\times 10^{-3}$)
	n_b	$CPE_b\text{-}T$ ($\mu\text{F cm}^{-2} \text{s}^{n-1}$)	R_b ($M\Omega\text{cm}^2$)	n_i	$CPE_i\text{-}T$ ($\mu\text{F cm}^{-2} \text{s}^{n-1}$)	R_i ($k\Omega\text{cm}^2$)		
Anodized 0.5CS-30V-3 min	0.97	42.96	220.00	0.91	249.50	7.14	220.00	0.50
0.5CS-30V-3 min	0.94	53.42	33.01	0.64	129.69	18.02	33.01	0.66
Anodized Ti	0.91	29.55	150.95	0.78	72.94	0.77	150.95	1.22

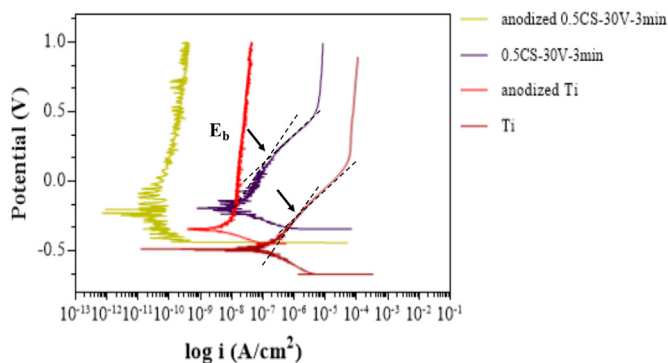


Fig. 13. Potentiodynamic polarization plots of the anodized 0.5CS-30V-3 min sample compared to the anodized Ti, 0.5CS-30V-3 min and pure Ti.

Table 5
Passivation current density, corrosion potential and breakdown potential of the coating.

Sample name	i_p ($\text{nA}\cdot\text{cm}^{-2}$)	E_{corr} (V vs. SCE)	E_b (V vs. SCE)
Anodized 0.5CS-30V-3 min	0.054	-0.23	-
0.5CS-30V-3 min	21	-0.2	0.13
Anodized Ti	10.3	-0.34	-
Ti	200	-0.48	-0.22

has more effectively prevented the localized corrosion of the substrate as it showed the highest E_b value (see Table 3).

3.3. The effect of anodized interlayer on nanocomposite coating properties

According to our results, the nanocomposite coating containing 0.5 mg/ml chitosan (0.5CS-30V-3 min) revealed the highest coating thickness and appropriate pore size as well as a better barrier property. Therefore, this coating was selected as the optimized coating, applied on the anodized surface of Ti. Fig. 10a shows the SEM image of the anodized Ti which entirely covered by titanium nanotubes (TiNTs). The average inner diameter and the wall thickness of the TiNTs were $82 \pm 19 \text{ nm}$ and $23 \pm 9 \text{ nm}$, respectively. Previous researches showed that the TiNT with the internal diameter between 70 and 100 nm could provide excellent biocompatibility leading to an improved cell proliferation [53,54].

After the formation of TiNT on the Ti surface, the chitosan reinforced HA-GO nanocomposite coating (0.5CS-30V-3 min) was applied on this surface (Fig. 10b). SEM image of the double layer nanocomposite coating (anodized 0.5CS-30V-3 min) showed the similar morphology as that of 0.5CS-30V-3 min. Cross-section image of the anodized 0.5CS-30V-3 min is presented in Fig. 10c. The thickness of the coating layer was estimated as $27.5 \pm 7.5 \mu\text{m}$. Compared to the 0.5CS-30V-3 min, the thickness was approximately equal, but less porosity and cracks were detected. To evaluate the distribution of elements in the cross-section of coating, EDX analysis was performed (Fig. 10d).

Our results demonstrated that the formation of TiNT did not have a significant role on deposition rate of HA nanopowder during the EPD process. The HA nanopowder with calcium to phosphorus ratio of 1.68 was uniformly distributed in whole coating thickness. Moreover, detachment of the coating layer was not identified which confirmed appropriate adhesion between the coating and anodized substrate surface. Adhesion strength of the nanocomposite coating deposited on Ti and anodized Ti was evaluated using the adhesion test. According to Fig. 11, while the adhesion of the 0.5CS-30V-3 min nanocomposite coating on the activated titanium was in the 2B class, it was improved to 4B class on the anodized titanium (anodized 0.5CS-30V-3 min), confirming the effective role of anodizing treatment on improving the adhesion strength of the coating. Mollie et al. [55] applied chitosan-based nanocomposite coating on the titanium substrate by EPD technique, and similarly showed the adhesion strength of 2B. Yan et al. [21] showed similarly that the formation of TiNT on the surface resulted in improved adhesion of HA-gelatin-GO composite coating to the substrate.

The EIS analysis was also performed on the anodized and consequently coated sample (anodized 0.5CS-30V-3 min) and the Nyquist and Bode plots were reported (Fig. 12a and b). The proposed equivalent electrical circuit was similar to that of 0.5CS-30V-3 min sample (Fig. 8c). The elemental values obtained by the selected circuit are presented in Table 4. The anodized 0.5CS-30V-3 min sample revealed the highest impedance and therefore revealed the best barrier performance. Moreover, the anodized 0.5CS-30V-3 min sample showed the highest total resistance (R_{tot}) about $220 M\Omega\text{cm}^{-2}$, which is about 6.7 times higher than that of 0.5CS-30V-3 min sample. According to the Bode-angle diagram (Fig. 12b), the plateau region at low frequencies can be observed around 80° for the anodized 0.5CS-30V-3 min sample, which is higher than the others, confirming the better diffusion barrier effect of this coating.

Corrosion behavior of coating was also investigated using potentiodynamic polarization test (Fig. 13) and the passivation current density and corrosion potential are summarized in Table 5. The results showed that the nanocomposite coating developed on the anodized Ti substrate revealed a passive current density of about $0.054 \text{ nA}/\text{cm}^2$ which is significantly lower than the Ti substrate with a current density of about $200 \text{ nA}/\text{cm}^2$. According to Yan et al. [21], the production of TiNT on the Ti substrate surface enhanced the bonding of the top coating leading to the high strength of adhesion. Therefore, the anodized layer not only enhanced the barrier property of the coatings, but also effectively prevented the occurrence of localized corrosion on the Ti substrate, as no breakdown potential was seen.

4. Conclusions

Novel and uniform nanocomposite coatings of chitosan reinforced hydroxyapatite (HA)-graphene oxide (GO) (CS-GO-HA) containing various amounts of chitosan were successfully applied on Ti substrate using electrophoretic deposition technique. The role of two layers of titanium oxide nanotube (TiNT) and CS-GO-HA on the physical and electrochemical properties of Ti substrate was evaluated. Increasing the amounts of chitosan content led to a reduction in deposition rate of HA-GO nanopowder as well as thickness and pore size of the coatings and

also encouraged the formation of micro-cracks. The water contact angle reduced with increasing the chitosan content, while apatite formation ability in the SBF solution and cell viability reduced. The cell viability significantly reduced from 119.3 ± 5.1 (% control) to 51.9 ± 14.8 (% control), when the chitosan concentration raised from 0.5 to 1.5 mg/ml after the first day of culture. Furthermore, the corrosion evaluation revealed a better barrier property for the chitosan-HA-GO coating containing 0.5 mg/ml chitosan.

The presence of TiNT as the intermediate layer successfully resulted in the formation of uniform and crack-free chitosan-HA-GO coating with the thickness of about $27.5 \pm 7.5 \mu\text{m}$. The TiNT intermediate layer provided improved adhesion of the coating to substrate leading to better passivation behavior. Our results concluded that the two-step anodizing and electrophoretic deposition of chitosan-HA-GO nanocomposite might be a promising implant coating material. However, extend in vivo studies are necessary to confirm this application. To conclude, the fabricated nanocomposite coating could be suggested as a novel bioactive and corrosion resistant layer for bone implant application.

References

- [1] M. Mehrali, A.R. Akhiani, S. Talebian, M. Mehrali, S.T. Latibari, A. Dolatshahi-Pirouz, H.S.C. Metselaer, Electrophoretic deposition of calcium silicate-reduced graphene oxide composites on titanium substrate, *J. Eur. Ceram. Soc.* (2) (2016) 319–332.
- [2] K. De Groot, R. Geesink, C.P.A.T. Klein, P. Serekian, Plasma sprayed coatings of hydroxylapatite, *J. Biomed. Mater. Res. A* 21 (1987) 1375–1381.
- [3] D. Morin, R. DeLong, W.H. Douglas, Clinical science cusp reinforcement by the acid-etch technique, *J. Dent. Res.* 63 (1984) 1075–1078.
- [4] C. Yao, T.J. Webster, Anodization: a promising nano-modification technique of titanium implants for orthopedic applications, *J. Nanosci. Nanotechnol.* 6 (2006) 2682–2692.
- [5] Y.T. Zhao, Z. Zhang, Q.X. Dai, D.Y. Lin, S.M. Li, Microstructure and bond strength of HA (+ ZrO₂ + Y₂O₃)/Ti6Al4V composite coatings fabricated by RF magnetron sputtering, *Surf. Coat. Technol.* 200 (2006) 5354–5363.
- [6] S. Lopez-Esteban, E. Saiz, S. Fujino, T. Oku, K. Suganuma, A.P. Tomsia, Bioactive glass coatings for orthopedic metallic implants, *J. Eur. Ceram. Soc.* 23 (2003) 2921–2930.
- [7] M. Afshar-Mohajer, A. Yaghoubi, S. Ramesh, A.R. Bushroa, K.M.C. Chin, C.C. Tin, W.S. Chiu, Electrophoretic deposition of magnesium silicates on titanium implants: ion migration and silicide interfaces, *Appl. Surf. Sci.* 307 (2014) 1–6.
- [8] W. Xue, X. Liu, X.B. Zheng, C. Ding, In vivo evaluation of plasma-sprayed wollastonite coating, *Biomaterials* 26 (2005) 3455–3460.
- [9] J.R. Woodard, A.J. Hilldore, S.K. Lan, C.J. Park, A.W. Morgan, J.A.C. Eurell, S.G. Clark, M.B. Wheeler, R.D. Jamison, A.J.W. Johnson, The mechanical properties and osteoconductivity of hydroxyapatite bone scaffolds with multi-scale porosity, *Biomaterials* 28 (2007) 45–54.
- [10] M. Li, Q. Liu, Z. Jia, X. Xu, Y. Cheng, Y. Zheng, T. Xi, S. Wei, Graphene oxide/hydroxyapatite composite coatings fabricated by electrophoretic nanotechnology for biological applications, *Carbon* 67 (2014) 185–197.
- [11] S. Mahmoodi, L. Sorkhi, M. Farrokhi-Rad, T. Shahabi, Electrophoretic deposition of hydroxyapatite-chitosan nanocomposite coatings in different alcohols, *Surf. Coat. Technol.* 216 (2013) 106–114.
- [12] X. Pang, I. Zhitomirsky, Electrodeposition of composite hydroxyapatite-chitosan films, *Mater. Chem. Phys.* 94 (2005) 245–251.
- [13] R. Ma, Y. Li, I. Zhitomirsky, Electrophoretic deposition of hyaluronic acid and composite films for biomedical applications, *JOM* 62 (2010) 72–75.
- [14] R. Ma, R.F. Epanand, I. Zhitomirsky, Electrodeposition of hyaluronic acid and hyaluronic acid-bovine serum albumin films from aqueous solutions, *Colloids Surf. B: Biointerfaces* 77 (2010) 279–285.
- [15] M. Cheong, I. Zhitomirsky, Electrodeposition of alginate acid and composite films, *Colloids Surf. A Physicochem. Eng. Asp.* 328 (2008) 73–78.
- [16] F. Sun, X. Pang, I. Zhitomirsky, Electrophoretic deposition of composite hydroxyapatite-chitosan-heparin coatings, *J. Mater. Process. Technol.* 209 (2009) 1597–1606.
- [17] A. Janković, S. Eraković, M. Mitrić, I.Z. Matić, Z.D. Juranić, G.C. Tsui, C. Tang, V. Mišković-Stanković, K.Y. Rhee, S.J. Park, Bioactive hydroxyapatite/graphene composite coating and its corrosion stability in simulated body fluid, *J. Alloys Compd.* 624 (2015) 148–157.
- [18] C. Wen, X. Zhan, X. Huang, F. Xu, L. Luo, C. Xia, Characterization and corrosion properties of hydroxyapatite/graphene oxide bio-composite coating on magnesium alloy by one-step micro-arc oxidation method, *Surf. Coat. Technol.* 317 (2017) 125–133.
- [19] A.A. White, S.M. Best, I.A. Kinloch, Hydroxyapatite-carbon nanotube composites for biomedical applications: a review, *Int. J. Appl. Ceram. Technol.* 4 (2007) 1–13.
- [20] F. Ordikhani, M.R. Farani, M. Dehghani, E. Tamjid, A. Simchi, Physicochemical and biological properties of electrodeposited graphene oxide/chitosan films with drug-eluting capacity, *Carbon* 84 (2015) 91–102.
- [21] Y. Yan, X. Zhang, H. Mao, Y. Huang, Q. Ding, X. Pang, Hydroxyapatite/gelatin functionalized graphene oxide composite coatings deposited on TiO₂ nanotube by electrochemical deposition for biomedical applications, *Appl. Surf. Sci.* 329 (2015) 76–82.
- [22] C. Wan, M. Frydrych, B. Chen, Strong and bioactive gelatin-graphene oxide nanocomposites, *Soft Matter* 7 (2011) 6159–6166.
- [23] C. Wan, B. Chen, Poly (ϵ -caprolactone)/graphene oxide biocomposites: mechanical properties and bioactivity, *Biomed. Mater.* 6 (2011) 055010.
- [24] H. Porwal, S. Grasso, M.J. Reece, Review of graphene-ceramic matrix composites, *Adv. Appl. Ceram.* 112 (2013) 443–454.
- [25] A. Lahiji, A. Sohrabi, D.S. Hungerford, C.G. Frondoza, Chitosan supports the expression of extracellular matrix proteins in human osteoblasts and chondrocytes, *J. Biomed. Mater. Res.* 51 (2000) 586–595.
- [26] J.D. Bumgardner, B.M. Chesnutt, Y. Yuan, Y. Yang, M. Appleford, S. Oh, R. McLaughlin, S.H. Elder, J.L. Ong, The integration of chitosan-coated titanium in bone: an in vivo study in rabbits, *Implant. Dent.* 16 (2007) 66–79.
- [27] M. Guglielmi, Sol-gel coatings on metals, *J. Sol-Gel Sci. Technol.* 8 (1997) 443–449.
- [28] K. De Groot, R. Geesink, C.P.A.T. Klein, P. Serekian, Plasma sprayed coatings of hydroxylapatite, *J. Biomed. Mater. Res. A* 21 (1987) 1375–1381.
- [29] Y.W. Song, D.Y. Shan, E.H. Han, Electrodeposition of hydroxyapatite coating on AZ91D magnesium alloy for biomaterial application, *Mater. Lett.* 62 (2008) 3276–3279.
- [30] L. Besra, M. Liu, A review on fundamentals and applications of electrophoretic deposition (EPD), *Prog. Mater. Sci.* 52 (2007) 1–61.
- [31] N. Iqbal, R. Nazir, A. Asif, A.A. Chaudhry, M. Akram, G.Y. Fan, A. Akram, R. Amin, S.H. Park, R. Hussain, Electrophoretic deposition of PVA coated hydroxyapatite on 316L stainless steel, *Curr. Appl. Phys.* 12 (2012) 755–759.
- [32] M. Javidi, S. Javadpour, M.E. Bahrololoom, J. Ma, Electrophoretic deposition of natural hydroxyapatite on medical grade 316L stainless steel, *Mater. Sci. Eng. C* 28 (2008) 1509–1515.
- [33] M. Li, Q. Liu, Z. Jia, X. Xu, Y. Shi, Y. Cheng, Y. Zheng, T. Xi, S. Wei, Electrophoretic deposition and electrochemical behavior of novel graphene oxide-hyaluronic acid-hydroxyapatite nanocomposite coatings, *Appl. Surf. Sci.* 284 (2013) 804–810.
- [34] R.A. Surmenev, M.A. Surmeneva, A.A. Ivanova, Significance of calcium phosphate coatings for the enhancement of new bone osteogenesis—a review, *Acta Biomater.* 10 (2014) 557–579.
- [35] J. Lausmaa, Mechanical, thermal, chemical and electrochemical surface treatment of titanium, *In Titanium in Medicine*, 2001, pp. 231–266.
- [36] A.K. Sharma, Anodizing titanium for space applications, *Thin Solid Films* 208 (1992) 48–54.
- [37] H. Mokhtari, Z. Ghasemi, M. Kharaziha, F. Karimzadeh, F. Alihosseini, Chitosan-58S bioactive glass nanocomposite coatings on TiO₂ nanotube: structural and biological properties, *Appl. Surf. Sci.* 441 (2018) 138–149.
- [38] N. Golaflshan, M. Kharaziha, M.H. Fathi, Tough and conductive hybrid graphene-PVA: alginate fibrous scaffolds for engineering neural construct, *Carbon* 111 (2017) 752–763.
- [39] S. Yu, J. Liu, W. Zhu, Z.T. Hu, T.T. Lim, X. Yan, Facile room-temperature synthesis of carboxylated graphene oxide-copper sulfide nanocomposite with high photodegradation and disinfection activities under solar light irradiation, *Sci. Rep.* 5 (2015) 16369.
- [40] Y.Y. Shi, M. Li, Q. Liu, Z.J. Jia, X.C. Xu, Y. Cheng, Y.F. Zheng, Electrophoretic deposition of graphene oxide reinforced chitosan-hydroxyapatite nanocomposite coatings on Ti substrate, *J. Mater. Sci. Mater. Med.* 27 (2016) 48.
- [41] Y.X. Pang, X. Bao, Y. Pang, X. Bao, Influence of temperature, ripening time and calcination on the morphology and crystallinity of hydroxyapatite nanoparticles, *J. Eur. Ceram. Soc.* 23 (2003) 1697–1704.
- [42] K.P. Sanosh, M.C. Chu, A. Balakrishnan, T.N. Kim, S.J. Cho, Preparation and characterization of nano-hydroxyapatite powder using sol-gel technique, *Bull. Mater. Sci.* 32 (2009) 465–470.
- [43] V.M. Correlo, E.D. Pinho, I. Pashkuleva, M. Bhattacharya, N.M. Neves, R.L. Reis, Water absorption and degradation characteristics of chitosan-based polyesters and hydroxyapatite composites, *Macromol. Biosci.* 7 (2007) 354–363.
- [44] X. Yang, Y. Tu, L. Li, S. Shang, X.M. Tao, Well-dispersed chitosan/graphene oxide nanocomposites, *ACS Appl. Mater. Interfaces* 2 (2010) 1707–1713.
- [45] Y. Tong, S. Bohm, M. Song, Graphene based materials and their composites as coatings, *J. Nanosci. Nanotechnol.* 1 (2013) 2381–8956.
- [46] A. Balamurugan, G. Balossier, S. Kannan, S. Rajeswari, Elaboration of sol-gel derived apatite films on surgical grade stainless steel for biomedical applications, *Mater. Lett.* 60 (2006) 2288–2293.
- [47] M. Bohner, J. Lemaître, Can bioactivity be tested in vitro with SBF solution? *Biomaterials* 30 (2009) 2175–2179.
- [48] R. Torkaman, S. Darvishi, M. Jokar, M. Kharaziha, M. Karbasi, Electrochemical and in vitro bioactivity of nanocomposite gelatin-forsterite coatings on AISI 316 L stainless steel, *Prog. Org. Coat.* 103 (2017) 40–47.
- [49] M. Sato, R. Tu, T. Goto, K. Ueda, T. Narushima, Apatite formation behavior on bio-ceramic films prepared by MOCVD, *J. Ceram. Soc. Jpn.* 117 (2009) 461–465.
- [50] O. Peitl, E.D. Zanotto, L.L. Hench, Highly bioactive P2O₅-Na₂O-CaO-SiO₂ glass-ceramics, *J. Non-Cryst. Solids* 292 (2001) 115–126.
- [51] A. Hakimzad, K. Raeissi, F. Ashrafzadeh, A comparative study of corrosion performance of sealed anodized layers of conventionally colored and interference-colored aluminum, *Surf. Coat. Technol.* 206 (2012) 4628–4633.
- [52] P. Su, X. Wu, Y. Guo, Z. Jiang, Effects of cathode current density on structure and corrosion resistance of plasma electrolytic oxidation coatings formed on ZK60 Mg alloy, *J. Alloys Compd.* 475 (2009) 773–777.
- [53] E. Gongadze, D. Kabaso, S. Bauer, T. Sliivnik, P. Schmuki, U.V. Rienen, A. Igljič, Adhesion of osteoblasts to a nanorough titanium implant surface, *Int. J.*

- Nanomedicine 6 (2011) 1801.
- [54] Y. Wang, C. Wen, P. Hodgson, Y. Li, Biocompatibility of TiO₂ nanotubes with different topographies, *J. Biomed. Mater. Res. A* 102 (2014) 743–751.
- [55] A. Molaie, A. Amadeh, M. Yari, M. Reza Afshar, Structure, apatite inducing ability, and corrosion behavior of chitosan/halloysite nanotube coatings prepared by electrophoretic deposition on titanium substrate, *Mater. Sci. Eng. C* 59 (2016) 740–747.